Journal of Materials Science & Technology 110 (2022) 269–282

Contents lists available at ScienceDirect

Journal of Materials Science & Technology

journal homepage: www.elsevier.com/locate/jmst

Research Article

High throughput synthesis enabled exploration of CoCrFeNi-based high entropy alloys

L. Zhao[a], L. Jiang[b], L.X. Yang[a], H. Wang[a], W.Y. Zhang[c], G.Y. Ji[b], X. Zhou[d], W.A. Curtin[d], X.B. Chen[e], P.K. Liaw[f], S.Y. Chen[b,*], H.Z. Wang[a,*]

[a] Beijing Advanced Innovation Center for Materials Genome Engineering, Beijing Key Laboratory of Metal Materials Characterization, Central Iron and Steel Research Institute, Beijing 100081, China
[b] Institute for Advance Studies in Precision Materials, Yantai University, Yantai 264005, China
[c] National Center for Materials Service Safety, University of Science and Technology Beijing, Beijing 100083, China
[d] Laboratory for Multiscale Mechanics Modeling, Ecole Polytechnique Federale de Lausanne, Lausanne CH-1015, Switzerland
[e] School of Engineering, RMIT University, Melbourne 3046, Australia
[f] Department of Materials Science and Engineering, The University of Tennessee, 37996, USA

ARTICLE INFO

Article history:
Received 5 July 2021
Revised 2 September 2021
Accepted 5 September 2021
Available online 28 November 2021

Keywords:
High-entropy alloys
High-throughput
Composition-structure-property

ABSTRACT

To accelerate the exploration, screening, and discovery of structural high-entropy alloys with targeted properties, the newly developed High-Throughput Hot-Isostatic-Pressing based Micro-Synthesis Approach (HT-HIP-MSA) is employed to efficiently synthesize and characterize 85 combinatorial alloys in a 13-principal element alloying space. These CoCrFeNi-based high entropy alloys span 1 quaternary, 9 quinary, and 36 senary alloy systems, and their composition-structure-property relationships are characterized and analyzed experimentally and computationally. From the single-phase FCC CoCrFeNi alloy base, with Mn, Cu, Ti, Nb, Ta, Mo, W, Al, and Si as principal element alloying additions, we find (1) the extended Mn solubility in the single-phase FCC CoCrFeNi-Mn_x alloys, (2) the destabilizing behavior for most of the quinary and senary alloys, and (3) the distinctive solid-solution-strengthening effects in the alloys. In combining the computational methods, the HT-HIP-MSA can be systematic and economic to explore and refine the compositions, structures, and properties of structural high-entropy alloys.

1. Introduction

For structural alloys, there are two exciting trends in the past two decades. One is the fast-growing development of high-entropy alloys (HEAs), and the other is the accelerating advances in materials infrastructure via the Materials Genome initiative. Different from the conventional alloys with one or two principal elements, the HEAs contain five or more principal elements, which are also characterized as multi-principal-element alloys (MPEAs) or complex concentrated alloys (CCAs) [1,2]. This special way for alloy-design considerations provides the exciting opportunities to explore in the vast alloying-composition space with combinations and variations of different elements. For structural HEAs, it also poses a grand challenge to design promising alloys through seemingly limitless composition-processing-structure-property possibilities. To accelerate the discovery, understanding, and maturation of new materials, the Materials Genome is steadfastly advancing to provide new computational, experimental, and data tools. Concerning the broad HEA composition space, the high-throughput Materials Genome engineering tools have been increasingly applied for the research and development of HEAs aiming for desirable microstructures and properties (e.g., good ductility with high yield strength, great resistance to oxidation or corrosion).

To efficiently screen for promising structural HEAs with targeted properties, computational methods, such as first principle calculations [3], calculations of phase diagrams (CALPHAD) [4] and parametric criteria [5], have been proposed for the high-throughput large-scale screening of alloy compositions in the design of HEAs. Recently, the data-driven machine learning (ML) also entered the materials toolbox, e.g., it is utilized in combination with experimental design and feedback to search for high entropy alloys (HEAs) with higher hardness [6]. For these high-throughput computational and data-driven approaches, experiments are vital to verify, validate, and demonstrate promising HEA compositions by the computational design [7,8]. Furthermore, high-throughput synthesis approaches are used to increase efficacy in alloy pro-

* Corresponding authors.
E-mail addresses: sychen@ytu.edu.cn (S.Y. Chen), wanghaizhou@ncschina.com (H.Z. Wang).

https://doi.org/10.1016/j.jmst.2021.09.031
1005-0302/

cessing and screening. Laser additive manufacturing as an efficient rapid solidification technique is used for synthesizing bulk HEAs [9]. Combinatorial thin-film synthesis is used for the efficient formation and exploration of broad composition spread [10]. The rapid alloy prototyping (RAP) [11], as a semi-continuous high-throughput bulk sample preparation approach, can process tens of alloy compositions in parallel. Diffusion-multiples enable the formation and characterization of composition gradients covering alloying space of interest [12].

One of the earliest and the most investigated HEA compositions is Cantor alloy, the equiatomic CoCrFeNiMn HEA with a single FCC phase. With recent progress, the Cantor alloy has been extended to an expansive regime in a multicomponent composition space with a single- or near-single FCC structure. Specifically, this Cantor alloy regime is expanded in various ways: (1) additions, e.g., CoCrFeNiMnCu equiatomic and CoCrFeNiMnAlx non-equiatomic six-component single-phase alloys; (2) variations, i.e., $CoCrFeNiMn_x$ non-equiatomic FCC alloys; and (3) replacements, i.e., CrFeCoNiCu and TiCrFeCoNi quinary alloys [1]. However, even with the exceptional mechanical properties demonstrated in the Cantor alloy and its related alloys [13–15], the progress is still hindered by the lack of foundational data. Based on the HEA studies via experimental, theoretical, computational, and data-driven approaches, even for Cantor alloys, the high-throughput synthesis is called upon [4,16] to provide much needed new data, new phenomena, and new experience to probe and evaluate the enormous number of potential structural HEAs.

For structural HEAs, their composition-processing-structure-property relationships are more critical, and more complex. To overcome some of the shortcomings of the current high-throughput synthesis methods for structural HEA studies, we employ a new method, High-Throughput Hot-Isostatic-Pressing based Micro-Synthesis Approach (HT-HIP-MSA), where

- elemental powders are used to provide the design freedom for synthesizing combinatorial HEAs,
- Honeycomb-array structures are used to make separate HEAs with distinctive chemistries, to efficiently use powder for making the 4-mm cross-sectional diameter alloy samples. This honeycomb-array structure maintains structural integrity is scalable to larger sizes during processing, and enables the synthesis of multiple HEAs in parallel.
- HIPing the HEAs at the high temperature for a prolonged time to ensure the elemental consolidation and interdiffusion, to achieve the polycrystalline microstructure, and to maintain consistent processing conditions.

This HT-HIP-MSA enables us to integrate high-throughput characterization tools, computational tools, theoretical models, and existing data to explore the CoCrFeNi based HEAs, where

- Mn, Cu, Ti, Nb, Ta, Mo, W, Al, and Si are considered principal alloying additions for the CoCrFeNi-based quinary and senary HEAs,
- A total of 85 alloys spanning 1 quaternary, 9 quinary and 36 senary alloy systems are synthesized, characterized and explored systematically and efficiently,
- Processed by the common parallel HIPing, the composition-structure-property relationship are studied for 85 bulk alloys.

With the opportunities and challenges spurred by the HEAs with the wide space of compositions, to overcome the shortcomings of the traditional one-at-a-time experimental design algorithms, we present an integrated approach to explore and screen the CoCrFeNi-based HEA compositions with systematic high-throughput synthesis and characterization as well as modeling and analysis for the combinatorial design of 85 HEAs. This approach thus accelerates (1) the establishment of the composition-microstructure-properties relationships, (2) the efficient acquisition of large datasets, and (3) the direct observation of new phenomenon not only for exploring new structural HEAs but also for improving, verifying, and validating the related alloy theories and models.

2. Results

2.1. Combinatorial design and high-throughput synthesis of CoCrFeNi-based HEAs

CoCrFeNiMn and its derivatives exhibit interesting microstructures and outstanding performance, including superior strength at both ambient and cryogenic temperature, exceptional fracture toughness, excellent resistance to oxidation and corrosion [17–21]. Even though extensive efforts are highlighted on Cantor alloys, much of them are performed within a limited adventure into the alloying elements and composition ranges from this known single-phase HEA to investigate the microstructures and mechanical properties. This is largely due to not only the lack of the critical data of phase boundaries or mechanical properties, but also the added complexity from the varying processing methods and conditions. To accelerate the structural HEA exploration and design, the high-throughput experimental approach, HT-HIP-MSA, is developed and applied in conjunction with theoretical and computational approaches.

Hence, the equiatomic CoCrFeNi alloy base is selected to illustrate the efficacy of high throughput method, i.e., the HT-HIP-MSA, to systematically examine the various principal-element alloying effects on structures and properties and to efficiently screen the promising HEAs. With respect to the CoCrFeNi alloy base, there are nine principal element additions are considered, namely Mn, Cu, Ti, Nb, Ta, Mo, W, Al, and Si. In the quinary HEAs, the fifth principal element is added by the replacement alloying element, R (R includes Mn) with varying atomic ratio (x) in contrast to the Cantor alloy of CoCrFeNiMn. Furthermore, Mn and Cu are considered as base alloying elements. We select W, Nb, Ta, and Mo as the refractory alloying elements. Al and Si are selected as the lightweight alloying elements. The quinary alloys span 9 quinary alloy systems and 48 alloys with the fifth principal element addition ranging from 0.5 to 2.5 or 3 at a 0.5 interval in atomic ratios, as displayed in Fig. 1(a). Moreover, the senary alloys are designed by adding principal elements (A) to the CoCrFeNi-R alloys to make combinatorial equiatomic CoCrFeNi-R-A HEAs. These senary alloys are distributed in 36 alloy systems, as presented in Fig. 1(b). In this combinatorial alloy design, the total of 85 alloys, including the CoCrFeNi alloy, are aimed to the systematically study the effects of the most commonly used 9 principal elements (Mn, Cu, Al, Ti, Ta, Nb, W, Mo, and Si) and their composition variations on the structures and properties of HEAs.

2.2. Compositions and structures of the CoCrFeNi-based HEA library

As depicted by Charles Darwin in 1859 “the comb of the hive-bee, as far as we can see, is absolutely perfect in economizing labor and wax” [22], the marvel of the geometry of the honeycomb structure inspired us to make use of this structural design to house the bulk discrete-alloy-array containing 85 different HEAs, as depicted in Fig. 2(a, b). Each cell represents one HEA composition (Fig. 2(c–p)). Firstly, the honeycomb structure provides us the efficient use of powders, the maximized volume of each cell, the maximum number of cells, and the consistent shape of cells. Hence, the maximized number of cells allows more different HEA alloys to be accommodated in one sample. Secondly, the advancements of modern processing technologies allow us to employ the laser additive manufacturing to realize the desired honeycomb structure

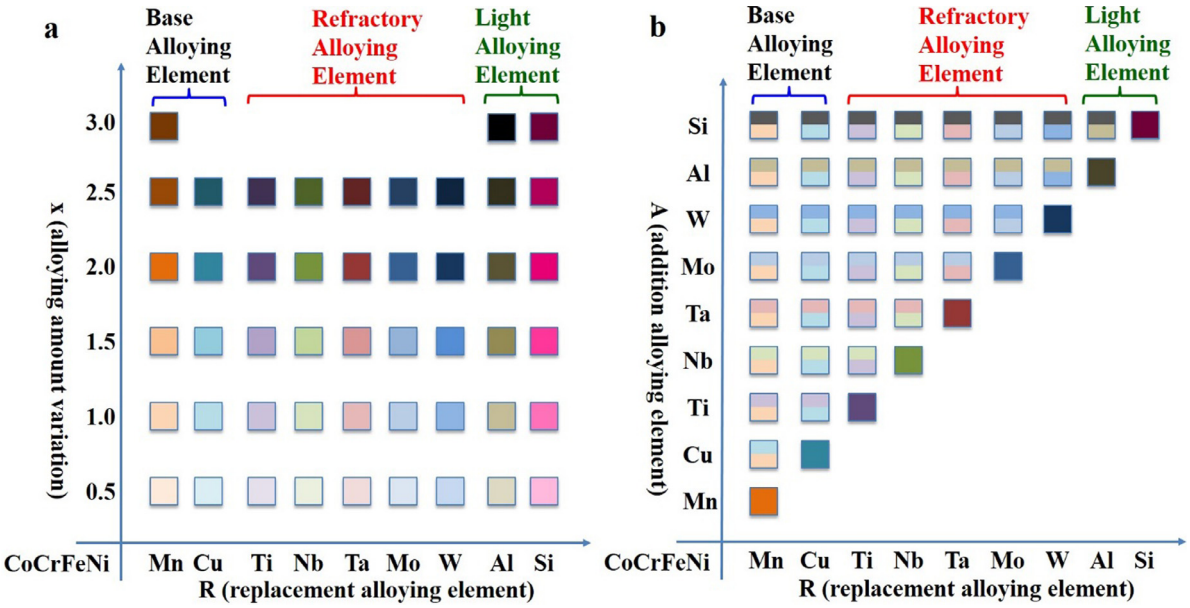

Fig. 1. CoCrFeMn-Based HEA design strategy: (a) CoCrFeNi-R_x, i.e., R (replacement alloying element) with *x* (alloying variation in atomic ratio); (b) CoCrFeNi-R-A (addition alloying element).

in precision, and the automated mechanical milling for simultaneously pre-mixing dozens of HEAs with starting elemental powder mixtures. After filling up each honeycomb cell with designed and pre-mixed powder compositions, HIP as the near-net-shape forming consolidation method is utilized to process in parallel the sealed honeycomb sample filled with designed HEA powder mixtures. Therefore, all 85 HEA compositions, which are processed in this manner, improves an order of magnitude savings in the HEA synthesis cycle time and cost, compared to the one-alloy-at-a-time synthesis approach. Thirdly, as displayed in Fig. 2(q), the HT-HIP-MSA processed 85 HEAs at 1000 °C for 4 h retained the hexagonal-shape cell structure as the original design, which is the key to reliably scale the sample size as per design and to effectively orchestrate the high-throughput characterization tools.

For high-throughput elemental characterization, μ-XRF with a spot size of 20 mm is automated to map the intensity distributions of 13 key elements over the entire surface of the HEA library sample consisting of 85 alloy compositions. The resultant elemental mapping (Fig. 2(d–p)) for 13 principal alloying elements reveals homogeneous elemental distributions of the HEA within the alloy cell. The SEM-EDS results (Fig. 2(q), Supplementary Table S1) show that the as-HIPed HEAs have actual chemical compositions of each alloy in reasonable agreement with the nominal design compositions, demonstrating the HT-HIP-MSA's processing capability and reliability.

As they dictate physical and mechanical properties of HEAs, chemistry-phase constitutions are of great importance to HEAs. However, many of them are unknown and cannot be reliably predicted. For the speedy characterization of the honeycomb-structured HEA library with 85 compositions, and further examine the reliability of the HT-HIP-MSA for HEAs, the μ-XRD is employed to automatically collect and analyze diffraction patterns. This high-throughput structure characterization technique collects the crystallographic structure data of 1 quaternary CoCrFeNi HEA (cell 1), 48 quinary CoCrFeNi-R_x HEAs (cells 2–49), and 36 senary CoCrFeNi-R-A HEAs (cells 50–85) (Fig. 3(a)) in less than 4 h. As a result, all the observed phases of 85 alloys are compared with the CALPHAD predictions and previous reports in Table 1. As expected, the quaternary CoCrFeNi HEA illustrates a single FCC phase, consistent with the results reported [23]. Surprisingly, CoCrFeNi-Mn_x HEAS retain single FCC phase with Mn addition ranging from 0.5 to 3 atomic ratio. Moreover, as Mn content increases, the corresponding major peak move to left, indicating the increasing lattice parameters, which is due to the large radius of Mn element. The CoCrFeNi-Cu_x alloys result in different thermodynamic properties compared with other CoCrFeNi-R_x alloys. The calculation and XRD result indicate that no intermetallic compounds are formed by Cu addition, but it tends to form two FCC (FCC1 and FCC2) solid solution phases, which can be attribute due to the large positive enthalpy of Cu with other component [24]. Al is another mostly studied alloying element in the CoCrFeNi. When Al increases from 0.5 to 3 atomic ratio, the primary phases of CoCrFeNi-Al_x alloys change from single FCC to FCC+BCC to BCC phase, which is also observed in literature [25] that Al destabilizes the FCC structure in the same HEA system. Similarly, for the CoCrFeNi base alloys with the addition of Nb, Mo, Ta, or W elements range from the 0.5 to 2.5 atomic ratio, the observed phases vary from FCC to FCC+BCC to Nb-, Mo-, Ta-, or W-rich BCC phase, which is due to the excess addition of these elements exceeding the solubility in the matrix. Moreover, excess Nb or Ta alloying additions encourage laves-phase formation in CoCrFeNi-Nb_x and -Ta_x HEAs, as both alloying additions can also be attributed to exceeding the solubility in the matrix [26]. The BCC solid solution phase and the tetragonal closed packing (TCP) μ phases (FeMo, FeW) are found in CoCrFeNi-Mo_x and -W_x alloys. Increasing Ti and Si elements from 0.5 to 2.5 atomic ratio leads to the phase formation from FCC to FCC+ complex intermetallics (IMs) to IMs. In Ti-containing HEAs, the negative enthalpy of Ti with Fe, Ni, and Cr promotes the formation of intermetallic B2 compounds and Laves phase together with BCC solid solution phase, which were predicted and experimentally verified [28,29] as well. It is suggested that the principal alloying element addition of Mo or Ti contributes to destabilizing the FCC solid solution and favoring the second-phase precipitation as also observed in the earlier XRD results [24].

Moreover, the high-throughput characterization reveals that when replacing element addition of -R_x extends to higher atomic ratio, the single-phase FCC CoCrFeNi base alloy structure will more likely be destabilized. For all 36 senary CoCrFeNi-R-A HEAs, the alloy structure is of a multiphase. For quinary CoCrFeNi-R_x HEAs, the

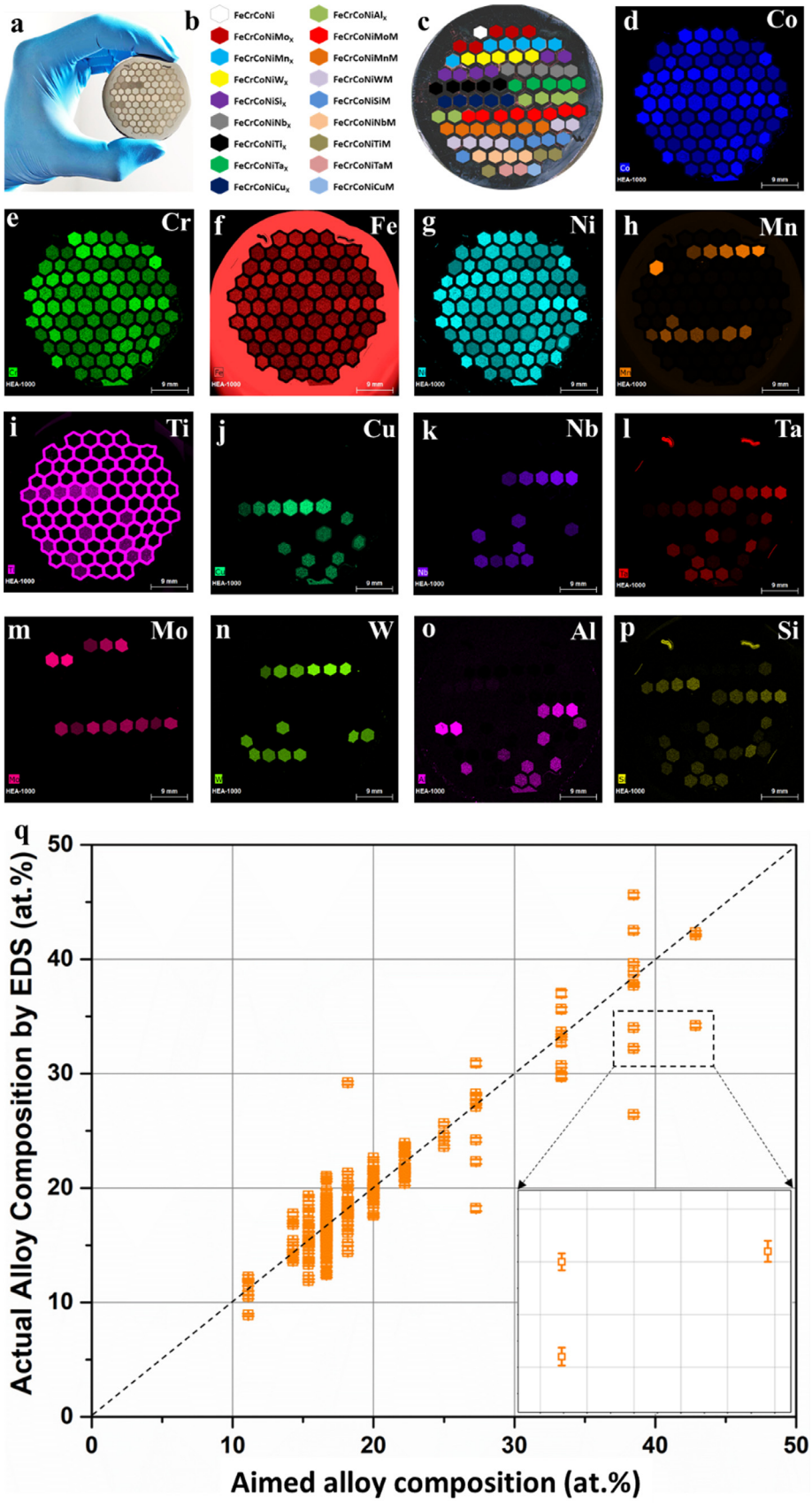

Fig. 2. (a–c) The design of honeycomb-structure; (d–p) The HIPed samples with 85 compositions; (q) The SEM-EDS results of 85 cells.

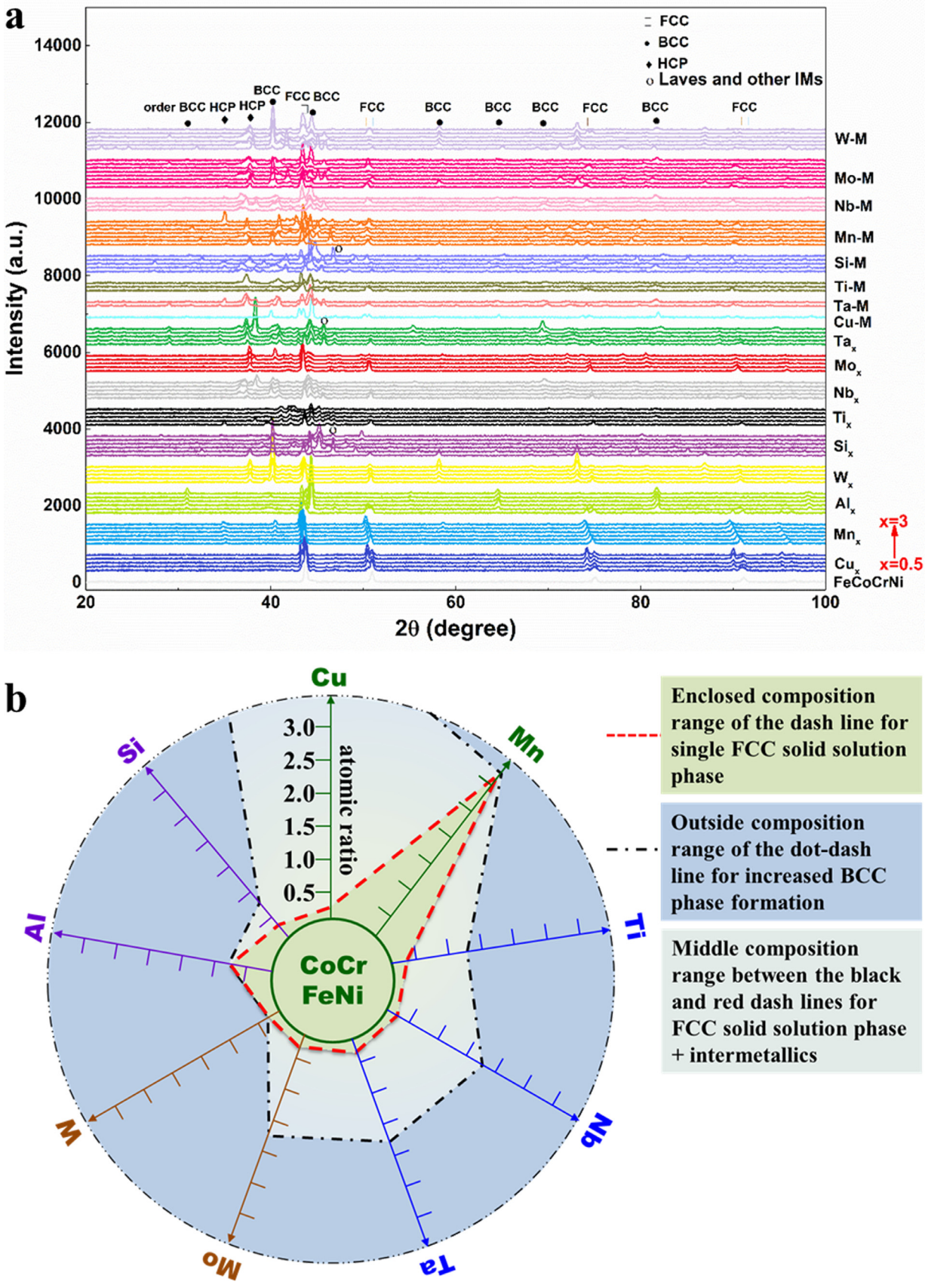

Fig. 3. (a) The XRD pattern of 85 alloys; (b) The classification of phases in quinary alloys.

Table 1
The summary of experimental phases, phases from literatures, phases by Calphad, experimental hardness, and calculated hardness.

Cell No.	Designed atomic percentage	Experimental Phases	Literature's Phases	Calculated phases	Experimental Hardness (HV)
1	$Fe_1Cr_1Co_1Ni_1$	FCC	FCC [1]	FCC	
2	$FeCrCoNiMo_{0.5}$	FCC+μ	FCC+σ [48]	FCC+σ	403
3	$FeCrCoNiMo_{1.0}$	FCC+μ	FCC+σ+μ [49] FCC+BCC+Laves [50]	FCC+σ	619
4	$FeCrCoNiMo_{1.5}$	FCC+μ	–	FCC+σ	783
5	$FeCrCoNiMo_{2.0}$	FCC+BCC (Mo) +μ	–	FCC+σ	845
6	$FeCrCoNiMo_{2.5}$	FCC+BCC (Mo) +μ	–	FCC+σ1+σ2	857
7	$FeCrCoNiMn_{0.5}$	FCC	–	FCC	268
8	$FeCrCoNiMn_{1.0}$	FCC	FCC [51]	FCC	266
9	$FeCrCoNiMn_{1.5}$	FCC	–	FCC	266
10	$FeCrCoNiMn_{2.0}$	FCC	–	FCC	254
11	$FeCrCoNiMn_{2.5}$	FCC	–	FCC	248
12	$FeCrCoNiMn_{3.0}$	FCC	–	FCC	251
13	$FeCrCoNiW_{0.5}$	FCC+BCC (W) +μ	FCC+μ [37]	FCC+σ+μ	410
14	$FeCrCoNiW_{1.0}$	FCC+BCC (W) +μ	–	FCC+σ+μ	550
15	$FeCrCoNiW_{1.5}$	FCC+BCC (W) +μ	–	–	539
16	$FeCrCoNiW_{2.0}$	FCC+BCC (W) +μ	–	σ+μ	693
17	$FeCrCoNiW_{2.5}$	FCC+BCC (W) +μ	–	BCC+σ+μ	648
18	$FeCrCoNiSi_{0.5}$	FCC+IM	$Si_{0.2}$ FCC+Unknown [52]	FCC+Cr_3Si	728
19	$FeCrCoNiSi_{1.0}$	BCC+IM	–	FCC+Co_2Si+Cr_3Si	748
20	$FeCrCoNiSi_{1.5}$	IM	–	BCC+Co_2Si+Cr_3Si	911
21	$FeCrCoNiSi_{2.0}$	IM	–	Co_2Si+Cr_3Si+MSi	727
22	$FeCrCoNiSi_{2.5}$	IM	–	Co_2Si+MSi+Cr_3Si	850
23	$FeCrCoNiSi_{3.0}$	IM	–	MSi+Co_2Si+Cr_3Si	912
24	$FeCrCoNiNb_{0.5}$	FCC+Laves	FCC+Laves [27]	FCC+Laves	441
25	$FeCrCoNiNb_{1.0}$	FCC+Laves	FCC+Laves [53]	FCC+Laves	588
26	$FeCrCoNiNb_{1.5}$	FCC+Laves	-	FCC+Laves	658
27	$FeCrCoNiNb_{2.0}$	BCC (Nb) +Laves	–	Laves	650
28	$FeCrCoNiNb_{2.5}$	BCC (Nb) +Laves	–	Laves+μ	627
29	$FeCrCoNiTi_{0.5}$	FCC+HCP	FCC+Laves+R+σ [29]	FCC+BCC+Ni3Ti	416
30	$FeCrCoNiTi_{1.0}$	FCC+BCC+IMs	FCC [54]	FCC+BCC+σ	627
31	$FeCrCoNiTi_{1.5}$	BCC+ IMs	–	BCC1+BCC2	652
32	$FeCrCoNiTi_{2.0}$	BCC+ IMs	–	BCC1+BCC2+Laves	690
33	$FeCrCoNiTi_{2.5}$	BCC+ IMs	–	BCC1+BCC2+Laves	665
34	$FeCrCoNiTa_{0.5}$	FCC+Laves	FCC+Laves [27]	FCC+Laves	458
35	$FeCrCoNiTa_{1.0}$	FCC+Laves	FCC+Laves [27]	FCC+σ+Laves	643
36	$FeCrCoNiTa_{1.5}$	FCC+Laves	–	BCC+Laves	740
37	$FeCrCoNiTa_{2.0}$	BCC+Laves	–	Laves	730
38	$FeCrCoNiTa_{2.5}$	BCC+Laves	–	Laves+μ	706
39	$FeCrCoNiCu_{0.5}$	FCC1+FCC2	FCC [55]	FCC1+FCC2	218
40	$FeCrCoNiCu_{1.0}$	FCC1+FCC2	FCC1+FCC2 [35]	FCC1+FCC2	196
41	$FeCrCoNiCu_{1.5}$	FCC1+FCC2	–	FCC1+FCC2	184
42	$FeCrCoNiCu_{2.0}$	FCC1+FCC2	FCC1+FCC2 [56]	FCC1+FCC2	170
43	$FeCrCoNiCu_{2.5}$	FCC1+FCC2	Cu_4 FCC1+FCC2 [57]	FCC1+FCC2	160
44	$FeCrCoNiAl_{0.5}$	FCC	FCC [58] FCC+BCC [59]	FCC+BCC	332
45	$FeCrCoNiAl_{1.0}$	FCC+BCC+Order BCC	FCC+BCC [60]	BCC1+BCC2+σ	432
46	$FeCrCoNiAl_{1.5}$	BCC+Order BCC	BCC+OrderBCC [61]	BCC1+BCC2	463
47	$FeCrCoNiAl_{2.0}$	BCC+Order BCC	BCC+orderBCC [62]	BCC1+BCC2	481
48	$FeCrCoNiAl_{2.5}$	BCC+Order BCC	BCC [24]	BCC1+BCC3	478
49	$FeCrCoNiAl_{3.0}$	BCC+Order BCC	BCC [24]	BCC1+BCC3	535
50	FeCrCoNiMoMn	FCC+Oxide	FCC+BCC [63]	FCC+σ	479
51	FeCrCoNiMoW	FCC+BCC+Unknown	FCC+BCC [63]	BCC+FCC+σ	669
52	FeCrCoNiMoSi	FCC+HCP (Ni) +IM+Unknown	–	Cr_3Si+Co_2Si+σ	722
53	FeCrCoNiMoNb	Unknown	–	σ+Laves+Ni_3Nb	726
54	FeCrCoNiMoTi	FCC+BCC+HCP (Cr)	FCC+BCC [63]	BCC+Ni3Ti+σ	757
55	FeCrCoNiMoCu	FCC+Unknown	–	FCC1+FCC2+σ	391
56	FeCrCoNiMoTa	BCC(Mo)+FCC+HCP+Unknown	–	Laves+σ+μ+Ni3Ta	791
57	FeCrCoNiMoAl	BCC+σ	$Mo_{0.5}$Al BCC+σ [64]	BCC+σ	626
58	FeCrCoNiMnW	BCC (W) +FCC+HCP (Cr)	FCC+BCC [63]	FCC+BCC	453
59	FeCrCoNiMnSi	BCC+IM	–	FCC+Cr_3Si+MnNiSi	560
60	FeCrCoNiMnNb	FCC+HCP (Cr) +Unknown	–	FCC+Laves	549
61	FeCrCoNiMnTi	FCC+HCP (Mn) +IM	FCC [63]	FCC+BCC1+BCC2+σ	521
62	FeCrCoNiMnTa	FCC+BCC+HCP(Cr)+Unknown	–	FCC+σ+Laves	672
63	FeCrCoNiMnCu	FCC1(Cu)+FCC2	–	FCC1+FCC2	261
64	FeCrCoNiMnAl	FCC+BCC+Oxide	FCC+BCC [65]	BCC1+BCC2+σ	471
65	FeCrCoNiWSi	FCC+BCC+IM	–	FCC+Laves+Ni5Si2	737
66	FeCrCoNiWNb	BCC(W)+Unknown	–	FCC+Laves+μ	680
67	FeCrCoNiWTi	BCC(W)+HCP(Cr)	FCC+BCC [63]	BCC1+BCC2+Laves+Ni3Ti	735
68	FeCrCoNiWTa	BCC+Unknown	–	FCC+μ+σ+Laves	715
69	FeCrCoNiWCu	BCC+FCC+Unknown	–	FCC+μ+σ+CuB_A13	392
70	FeCrCoNiWAl	BCC(W)+BCC(Fe,Cr)+Unknown	–	BCC+R+μ+σ	566
71	FeCrCoNiSiNb	FCC +BCC+IM	–	Liquid+Laves+$M11Si_8$+Cr_3Si	794

(*continued on next page*)

Table 1 (*continued*)

Cell No.	Designed atomic percentage	Experimental Phases	Literature's Phases	Calculated phases	Experimental Hardness (HV)
72	FeCrCoNiSiTi	BCC(Fe,Cr)+FCC(Ti)+Oxide	–	Liquid+Laves+Cr_3Si+*G*	749
73	FeCrCoNiSiTa	BCC+IM+Unknown	–	Liquid+Laves+Cr_3Si	881
74	FeCrCoNiSiCu	FCC+IM	FCC1+FCC2+σ [66]	FCC1+FCC2+Co_2Si+Cr_3Si	574
75	FeCrCoNiSiAl	BCC+IM	BCC+σ [67]	BCC3+BCC2+Cr3Si+Co2Si	779
76	FeCrCoNiNbTi	BCC+IM	–	BCC+Laves+Ni3Ti	573
77	FeCrCoNiNbTa	BCC+IM+Unknown	–	Laves+σ+μ	650
78	FeCrCoNiNbCu	FCC+Laves+Unknown	- FCC+Laves [66]	FCC1+FCC2+Laves	438
79	FeCrCoNiNbAl	BCC+Unknown	BCC+Laves+B2 [68]	BCC1+BCC2+Laves	555
80	FeCrCoNiTiCu	FCC+Unknown	FCC+Laves [69]	BCC+FCC1+FCC2+σ+T6CuNiTi	488
81	FeCrCoNiTiAl	BCC	BCC1+BCC2 [70] BCC1+BCC2+Laves [54]	BCC1+BCC3	584
82	FeCrCoNiTiTa	FCC+BCC+HCP+Unknown	–	BCC+Laves+Liquid	680
83	FeCrCoNiTaCu	FCC+BCC+IM+Unknown	–	FCC1+FCC2+Laves+σ	485
84	FeCrCoNiTaAl	BCC +Oxide	–	BCC1+BCC3+Laves	614
85	FeCrCoNiAlCu	FCC1(Cu)+FCC2+BCC+IM	FCC+BCC [71]	FCC+BCC+σ+Liquid	385

formation of the FCC and BCC phases resulting from varying replacing elements is illustrated in Fig. 3(b). Clearly, the FCC solid solution is limited in the alloys with low concentrations of replacing element, but for CoCrFeNi-Mn_x HEAs, the FCC phase is maintained up to 3 atomic ratios of Mn. For CoCrFeNi-Ti_x, -Nb_x, -Ta_x and -Al_x HEAs, when the replacing element alloying additions increase to above 1.5 to 2 atomic ratios, the major structure change from the FCC to BCC phase. For CoCrFeNi-Si_x HEAs, when the Si addition is about 1.5 atomic ratio or more, the alloy structure becomes intermetallic completely. By integrating a high-throughput techniques of synthesizing and characterizing, we can efficiently obtain the composition-structure dataset for a wide range of HEA compositions, and the observed HEA phase constitution is consistent with the available literature data.

2.3. Composition and structure relationships of the CoCrFeNi-based HEA library

Phases formed in the present CoCrFeNi-based HEAs, as measured by the high-throughput XRD and summarized in Table 1, exhibit alloy structures ranging from single-phase solid solutions to complex structures with IMs. With elemental additions ranging from 0.5 to 3, combinatorial alloying additions of the 9 principal elements into the CoCrFeNi-based alloys above a certain level will induce the matrix phase transformation or precipitate new phases, e.g., the increased addition of Al or W will lead to the phase transformation from FCC to BCC phases. Only four types of alloy systems exhibit simple-single or dual-phase FCC solid solutions with the increased amounts of replacing elements, i.e., Mn_x, Al_x, Cu_x, and W_x. The other quinary or senary HEA systems present multiple complex phases, including B2, μ, σ, or Laves phases in a disordered solid solution, which can significantly affect the mechanical behaviors of such alloys. Additionally, oxide phases are also observed in few of the Mn-containing HEAs and possibly can be attribute to the powder contamination.

To screen alloy compositions, high-throughput computation methods integrating empirical rules, first-principal calculations, CALPHAD, and others are proposed to predict the solid-solution phase formation in HEAs in a fast and effective way. For an empirical approach, the Hume-Rothery rules are broadly applied in HEAs [30]. Due to the efficacy and success in composition-phase relation and alloy design studies, these rules are also used in the application of high-throughput investigations. Among the developed parameters of the Hume-Rothery rules, the atomic size difference ($_\delta$), the enthalpy of mixing (ΔH_{mix}), entropy of mixing (ΔS_{mix}), and an $\Omega = \frac{T_m S_{\mathrm{mix}}}{|\Delta H_{\mathrm{mix}}|}$, combining ΔH_{mix}, ΔS_{mix}, and melting temperature, T_m, are mostly applied [31]. These parameters are adopted in the present study to predict the solid solution (SS) or IM phases formation, and to compare with the experimental results (Supplementary Table S1). With increasing the amounts of alloying elements, the $_\delta$ value increases monotonically, while the Ω value presents an opposite trend. From Table S1, it is apparent that the studied HEAs are more likely to form FCC solid solutions with the small addition of an alloying element, which should be due to the FCC structure of the CoCrFeNi base alloy. With increasing the amounts of refractory metal of W, Ta, or Nb, the original FCC phase tends to transform to a BCC phase because of their BCC crystal structures of alloying elements.

Ω and $_\delta$ are highlighted as the combination of them is more effective in phase prediction, and the Ω was plotted against the $_\delta$ value to predict the IM or SS phases in HEAs, as presented in Fig. 4(a). According to the previous studies [31], the critical boundary of $_\delta = 6.6\%$ and $\Omega = 1.1$ are drawn to demarcate the location of the SS and *IMs* formation region. It is suggested that the solid solution and IMs domains could be successfully separated by the Ω and $_\delta$ values, i.e., $\Omega > 1$ and $_\delta < 6.6\%$ favor the formation of a single SS, while beyond this region, a complex IM tends to form. However, this empirical criterion breaks down compared to our experimental results as there are a large number of HEAs with SS plus IMs formation in the region of $\Omega > 1$ and $_\delta < 6.6\%$. Moreover, the domain of SS is overlapped by the SS+IMs area, as indicated in the Fig. 4. Actually, as in one of the HEA review [1], many HEAs favor the formation of the SS+IMs, rather than the single solid solution, which is largely due to the limited solubility, complex electronegativity, mixing enthalpy and other important interactions amongst the alloying components.

The average valence electron concentration (VEC) and itinerant electron, e/a, are other criteria employed to determine the structure and stability of solid solution alloys, similar to those composition-weighted terms of the Hume-Rothery rules, as described as below:

$$\mathrm{VEC} = \sum_{i=1} c_i \mathrm{VEC}_i \tag{1}$$

$$e/a = \sum_{i=1} c_i e/a_i \tag{2}$$

where VEC_i and e/a are the valence electron concentration and itinerant electron of the element, *i*, respectively [32]. They are usually intended to identify the crystal structure of the existing solid solutions when a limited number of alloys were considered within a given alloy family. The examined e/a in a quinary system were plotted against VEC and their corresponding experimental structure, as shown in Fig. 4(b). As seen in Fig. 4(b), Nb- and Mo-containing alloys display different trends of solid-solution formation from other replacing elements with the variation of e/a and

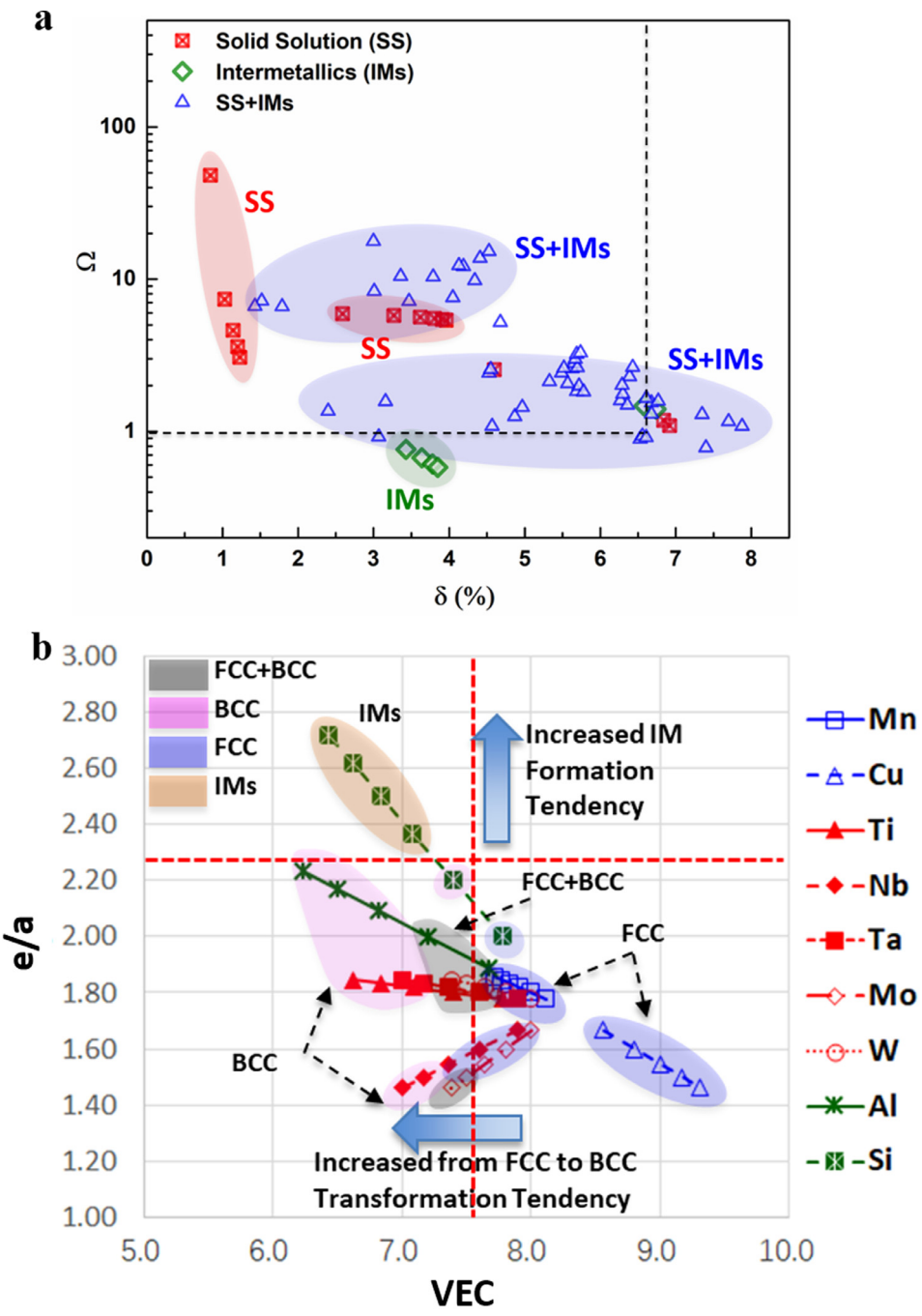

Fig. 4. (a) Phase formation determined by Ω and $_{\delta}$; (b) Phase classification determined by VEC and *e*/*a*.

VEC value. High *e*/*a* and VEC of *e*/*a* >1.55, VEC>7.6 result in an FCC-structured solid solution. Beyond this region, Nb and Mo alloys exhibit stable BCC and FCC+BCC structures, respectively.

While for Mn, Cu, Ti, Ta, W, Al, W, and Si alloys, an FCC structure is more likely to develop with high VEC and low *e*/*a* values, lying on the region with VEC > 7.6 and *e*/*a* < 1.88. As *e*/*a* increases and VEC decreases, the structure changes from an FCC + BCC dual phase to BCC solid solution, which is different from the previous investigation that an FCC structure is stable for VEC < 7.5 or 1.8 < *e*/*a*< 2.3 whereas an FCC structure develops for VEC >7.5 or 1.6<*e*/*a*<1.8 [11] or *e*/*a*<1.65 to be FCC, 1.65 < *e*/a < 2.05 a complex phase, and *e*/*a* > 2.05 is an BCC structure [33]. In Ti and Ta-containing alloys, the *e*/*a* is almost constant and the increasing the VEC value favors the formation of an FCC structure. In Si-containing alloys, only IM is found as *e*/*a* > 2.3 and VEC < 7.2. It is apparent that the fixed critical boundary of VEC or e/a cannot satisfactorily define all the HEA composition-structure relationships.

A more scientifically sound CALPHAD method with an assessed 26-element HEA database is applied in this study to evaluate the composition-phase constitutions. For the 13 principal alloying elements of our study are all in the HEA database as documented [34], where all the 78 related binaries are assessed in a full range, 82 out of 192 ternaries are assessed in a full range. Our evaluation reveals that the CALPAHD predictions matches nicely with the experimental observations of the major phases in HEAs, much better than empirical rules. However, with respect to the minor phases or second phases, such as σ or μ, the predicted and experimental results are mostly inconsistent. It should be noted that different

phases and various levels of decomposition and inhomogeneity are found in the similar HEAs in the literature data, which is likely because of the nonequilibrium state of studied alloys and the varied processing conditions. For example, the as-cast results overestimate the extent of SS. Such disadvantage can be avoided in the current high throughput experiment since all 85 alloys are synthesized and treated under the same processing conditions. Without added complexity due to processing, the composition effects on the phase formation or mechanical properties are obtained more consistently.

Based on these 9 replacing elements in CoCrFeNi-based HEAs, the transition among the FCC structure, FCC + BCC dual phase, and BCC structure in low and high-alloying element HEAs is experimentally evaluated and predicted by means CALPHD and empirical rules, which can serve as the guide to design the HEA compositions with targeted phases. It is suggested that all measured solid-solution alloys meet the two combined-parameter criteria of the empirical Hume-Rothery rules, but alloy predictions meeting these criteria are not always determined to be solid solutions, as illustrated in Fig. 4. As demonstrated by current experimental results, the empirical criterion is not always valid to predict the composition-phase constitutions in the HEAs, the CALPHAD approach with assessed database can reliably predict the major phases in the HEAs. Thus, our high-throughput approach is vital to efficiently identify the phase formation or mechanical properties of designed composition, and to provide large datasets with comparable processing conditions to improve the existing computational models and empirical rules and to develop new ones.

2.4. Mechanical properties of the CoCrFeNi-based HEA library

Automated micro-Vickers hardness experiments enable high-throughput testing of all 85 cells in the honeycomb-structured HEA library and can be conducted to effectively screen the promising compositions of HEAs based on hardness values. For 1 quaternary and 9 quinary HEA systems, varying trends in the hardness values of 45 representative individual HEAs are illustrated in Fig. 5(a). The quaternary base alloy, i.e., the CoCrFeNi HEA, exhibits a microhardness value of 245 HV. Regarding CoCrFeNi-R_x HEAs (R = Mo, Mn, W, Si, Nb, Ti, Ta, Cu, and Al, x = 0.5, 1.0, 1.5, 2.0, 2.5, and 3.0), there is a clear correlation between the hardness and molar fraction of alloying elements. As shown in Fig. 5, microhardness increases along with the increasing Mo and Al contents in both CoCrFeNi-Mo_x and CoCrFeNi-Al_x HEAs. In contrast, the additions of Mn and Cu reduce the hardness of the CoCrFeNi base alloy and show decreasing trends in both CoCrFeNi-Mn_x and CoCrFeNi-Cu_x HEAs. Moreover, a peak hardness value emerges in the CoCrFeNi-Ta_x, -W_x, -Ti_x, and Nb_x HEAs. Interestingly, the addition of Si imposes a less clear effect on the hardness of CoCrFeNi-Si_x HEAs. All the examined hardness values of 85 alloys in one sample was compared with the previously-investigated alloys from many different research groups, as presented in Table 1. The CoCrFeNi-based HEAs with contents of $Cu_{0.5}$, $Cu_{1.0}$, $Ta_{0.5}$, $W_{0.5}$, $Ti_{0.5}$, $Nb_{0.5}$, and $Nb_{1.0}$ in this investigation have similar hardness values to the reported ones [27,29,35–38]. It is noted that hardness values of all CoCrFeNi-Al_x, CoCrFeNi-Nb_x, CoCrFeNi-Ti_x, and CoCrFeNi-Mo_x HEAs are comparable with the values in the literature [39].The relationships between the addition of alloying elements and resulting hardness of all 36 senary CoCrFeNi-R-A HEAs (R, A = Mo, Mn, W, Si, Nb, Ti, Ta, Cu, and Al, respectively) are more complicated, which is exhibited in Fig. 5(b). The representative hardness values range from 260 to 880, as indicated by the colored legend. Some systems show clear trends, e.g., additions of Cu and Mn result in lower hardness, whilst additions of Si and Mo increase the hardness of HEAs.

As exhibited in Table 1, the hardness values of 85 alloys are effectively measured by the high-throughput methodology. The deviation of hardness in the current experiment from literatures could be due to the different casting, deformation process, or heat-treatment parameters that cannot be avoided in conventional experiments. Whereas in the current work, these processing variations are limited since all the 85 alloys are synthesized and treated at the same time in one sample, which can ensure the consistency of tested materials. These harnesses data enrich the information and knowledge of the designed compositions efficiently and reliably, and they also provide consistent datasets to verify and validate the theoretical simulation of hardness or strength.

Table 2
Apparent FCC volumes V_n for all alloying elements.

Element n	Apparent volume n (Å^3)
Ni	10.94 [45]
Co	11.12 [45]
Fe	12.09 [45]
Cr	12.27 [45]
Mn	12.60 [45]
Al	14.10*
Cu	12.80*(11.80 [43])
Mo	15.91*
Ti	16.02*

* indicates value calculated in this work.

To quantitatively understand the trends in hardness for the CoCrFeNi-R_x alloys, we apply the theory of Varvenne et al. [40–42] that has been used successfully for many alloys in the FCC Cantor alloy Co-Cr-Fe-Mn-Ni family. Within this framework, the zero-temperature yield shear stress τ_{y0} and energy barrier ΔE_b for dislocation motion in an FCC alloy are

$$\tau_{y0} = 0.049\left[\frac{\Gamma}{b^2}\right]^{\frac{-1}{3}}\left[\mu^V\frac{1+\nu^V}{1-\nu^V}\right]^{\frac{4}{3}}\left[\frac{2\sum_n c_n\Delta V_n^2}{9b^6}\right]^{\frac{2}{3}} \quad (3)$$

$$\Delta E_b = 2.58\left[\frac{\Gamma}{b^2}\right]^{\frac{1}{3}} b^3\left[\mu^V\frac{1+\nu^V}{1-\nu^V}\right]^{\frac{2}{3}}\left[\frac{2\sum_n c_n\Delta V_n^2}{9b^6}\right]^{\frac{1}{3}} \quad (4)$$

where b is the Burgers vector, $\{c_n\}$ the alloy composition, $\Gamma = 0.123\,\mu_{110/111}b^2$ the dislocation line tension with $\mu_{110/111} = (C_{11}-C_{12}+C_{44})/3$, and $\mu^V = \frac{C_{11}-C_{12}+3C_{44}}{5}$, $\nu^V = \frac{3B-2\mu^{Voigt}}{2(3B+\mu^{Voigt})}$, $B = (C_{11}+2C_{12})/3$ are the Voigt-averaged alloy elastic constants. Most importantly, ΔV_n is the misfit volume of element n in the alloy defined as $\Delta V_n = V_n - \sum_n c_n V_n$ where V_n is the apparent volume of element n. At temperature T and strain-rate $\dot{\varepsilon}$, the shear yield stress $\tau_y(T,\dot{\varepsilon})$ then follows as

$$\tau_y(T,\dot{\varepsilon}) = \tau_{y0}\exp\left(-\frac{1}{0.57}\frac{kT}{\Delta E_b}\ln\frac{\dot{\varepsilon}_0}{\dot{\varepsilon}}\right) \quad (5)$$

where k is Boltzmann constant and $\dot{\varepsilon}_0 = 10^4$/s a reference strain rate. This strengthening is the intrinsic strengthening and does not include finite-grain-size Hall-Petch effects.

For the CoCrFeNi-R_x alloys, we start with the apparent volumes for Co, Cr, Fe, Ni and Mn as derived by Varvenne et al. [40]. For each solute R, we consider the dilute composition c_R=0.033 corresponding to FCC CoCrFeNi-$R_{0.14}$ and compute the alloy elastic constants and apparent volume for R using first-principles DFT (details presented elsewhere). Changes to the elastic constants are small and not clearly correlated with R and so we use the values for the base alloy. The apparent volumes are shown in Table 2 and follow expected trends, although the Cu volume is somewhat larger than those of fcc Cu (11.80 Å^3) and Cu in RhIrPdPtNiCu (12.15) Å^3 [43].

Since hardness typically corresponds to the flow stress at ~10% plastic strain, a direct comparison of the theoretical yield strength and the measured hardness is not possible. We thus follow the strategy of Bracq et al. [42] and examine normalized quantities.

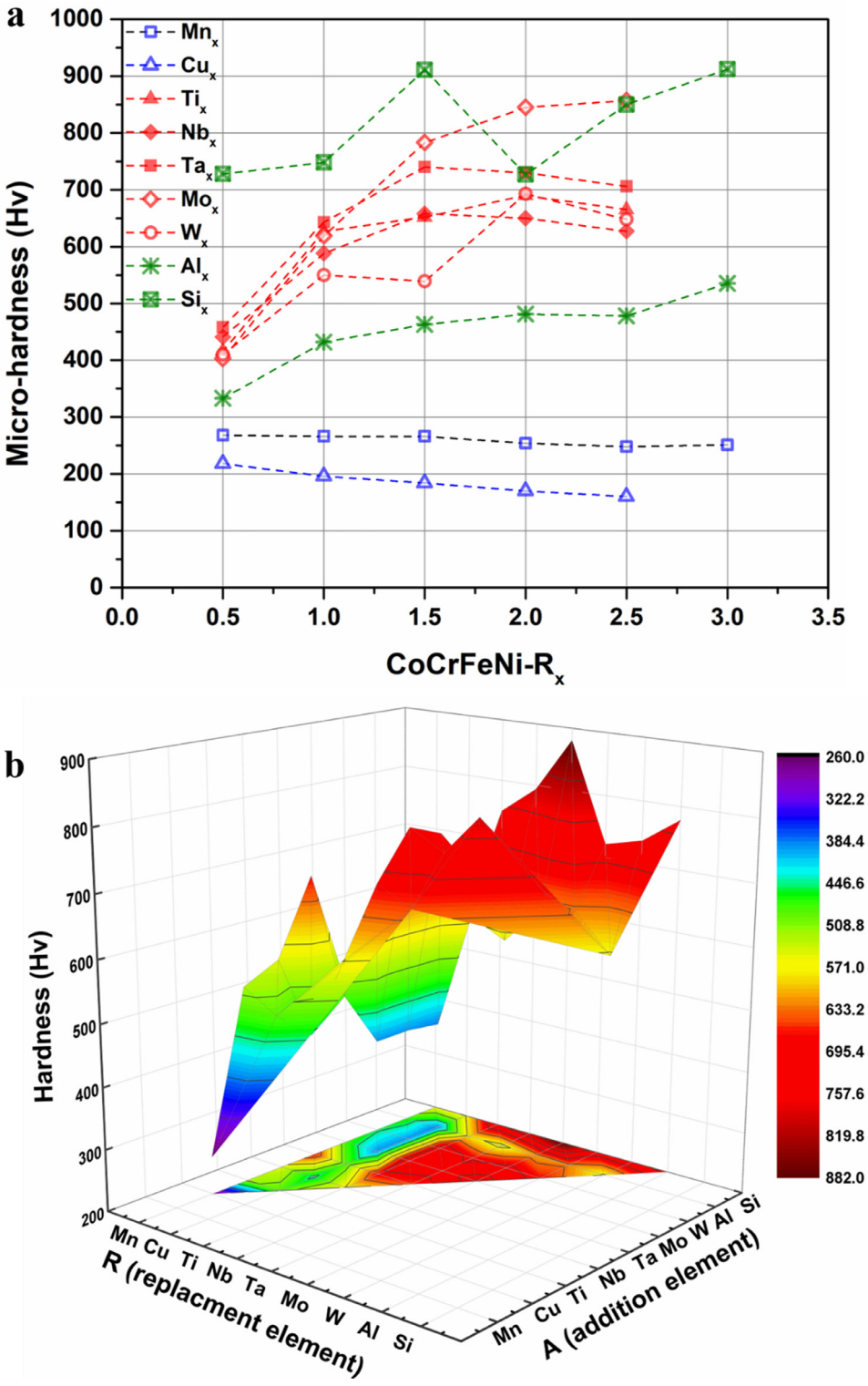

Fig. 5. (a) The microhardness variation with the CoCrFeNiR$_x$ (x = 0.5–3.0); (b) The microhardness variation with the CoCrFeNi-R-A.

The predicted yield strength of CoCrFeNi-R$_x$ is normalized by the yield strength of CoCrFeNi, $\tau_y(\text{CoCrFeNi}-\text{R}_x)/\tau_y(\text{CoCrFeNi})$. The experimental hardness 240 HV of CoCrFeNi suggests a grain-size Hall-Petch (H-P) hardening of 122 relative to the measured hardness 118 HV at infinite grain size [44]. The H-P contribution is typically weakly alloy-dependent [44]. For comparisons with the theory, we thus consider an HP-corrected and normalized hardness $(H_V - 122)/118$.

Fig. 6 shows the predicted normalized yield strength and the measured normalized/HP-corrected hardness versus composition x for R = Mn, Al, Cu, Mo and Ti at x = 0.25, 0.5 at T = 300 K and $\dot{\varepsilon} = 0.001$; note that the model assumes the alloys are FCC. Mn additions are observed and predicted to cause a slight increase in strengthening that is nearly constant over the composition range, consistent with previous results on the Cantor alloy CoCrFeMnNi [45]. With the DFT-estimated apparent volume, Cu ad-

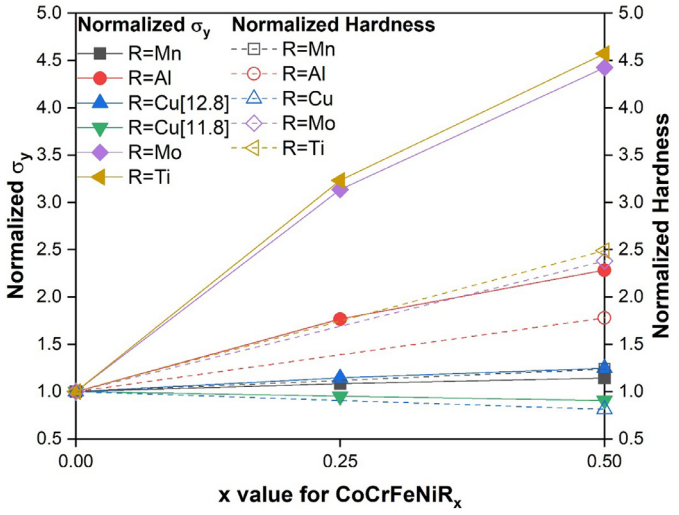

Fig. 6. Normalized yield strength predicted by solute-strengthening model and normalized hardness from experiment; For $CoCrFeNiCu_x$, the predictions from different apparent volumes (12.8 Å^3 and 11.8 Å^3) are both presented in the figure.

ditions are predicted to show a small strengthening while experiments show a slow decrease. Predictions using the apparent Cu volume of 11.80 Å^3 are, however, quite consistent with the experiments. Al additions create reasonable strengthening, as found in literature studies and as predicted [46], although the predictions are higher than experiments. Mo and Ti additions are predicted and observed to cause much higher strengthening even at low concentrations. The experimental hardness ratio is much lower than predicted, but these alloys are not single-phase FCC. The observed formation of the μ phase likely removes mainly Mo/Ti from the FCC lattice, leaving a matrix with lower Mo/Ti content and, hence, lower strength while the (large) μ –phase particles contribute little to strengthening.

The predictions here capture the major trends in hardening observed across the solutes *R* examined experimentally. Theory with high-throughput computations in the dilute limit can thus broadly identify attractive solutes for experimental study. However, high-throughput synthesis for the range of solutes identified theoretically remains essential to investigate single- vs. multiphase behavior and to quantitatively evaluate mechanical and other properties.

3. Discussion and conclusions

To evaluate HEAs for structural applications, it is vital to establish composition-process-structure-property relationships. The traditional approach, which often focuses on one principal element alloying at a time, is increasingly becoming a bottle neck to explore the vast multicomponent HEA space. In the present work, we draw on widely-studied CoCrFeNi-based HEAs with 9 replacing principal elements and spanning 9 quinary HEA systems and 36 senary HEA systems. To explore the composition-structure-property relationships including the crucial composition-phase limit and hardness in the vast space of multiple component compositions, the replacing principal elements vary in a relatively wide range from the 0.5 to 3 atomic ratio in the quinary CoCrFeNi-R_x alloys, and the replacing and additional principal elements represent all 36 R-A binary combinations in the senary CoCrFeNi-R-A alloys. Combinatorial pure elemental powder mixtures are prepared as designed and processed in single HIP experiment to produce 85 or more HEAs in one batch. This approach in fact realizes the HEA design freedom in elemental combinations and reduce complexity and limit variation due to processing. We explore the broad alloy composition space with efficient synthesis of bulk samples, acquiring composition-structure-hardness datasets for the HEA library. We identify the conditions of forming single -phase solid-solution HEAs, and verify the elemental effect on the phase stability and hardening. We characterize and analyze the composition-structure-property relationships experimentally and computationally.

The HT-HIP-MSA is demonstrated highly efficient in testing multiple hypothesis or elemental combination, aiming to find the hardening effects and phase-formation boundary, e.g., the appearance of the second-phase ($CoCrFeNi\text{-}Mo_x$) or the transition to another structure ($CoCrFeNi\text{-}Al_x$) in one sample. Based upon the current results, we will focus on CoCrFeNi-based HEA system with reduced alloying amount and varying elements to optimize HEAs for targeted applications. We will apply this high-throughput strategy to quickly capture the phases, mechanical properties, and their relationships of specific HEAs. Furthermore, in combining the computational methods, the HT-HIP-MSA offers a new strategy in designing and exploring new structural HEA compositions, and can be applied broadly to other alloy systems with significantly reduced cycle time and much lowered cost.

To explore the seemingly limitless compositional space of HEAs, it is of great importance to develop reliable and efficient theoretical, computational, and experimental approaches in evaluating and screening of HEA compositions. The present work presents an innovative High-Throughput Hot Isostatic Pressing (HIP) Micro-Synthesis Approach (HT-HIP-MSA) to realize a combinatorial design of 85 CoCrFeNi-based HEAs in a single sample and in a single processing cycle from elemental powders to alloys. To rapidly map the chemistries, structures, and mechanical properties of these HEAs, the alloys were characterized by micro X-ray fluorescence, micro X-ray diffraction, and micro Vickers hardness techniques in the high-throughput fashion. With the same controlled processing conditions, the resulting chemistry-structure-property data not only offers better evaluation and direct comparison of alloying effect on structures and properties from the selection or combination of Mn, Cu, Ti, Nb, Ta, Mo, W, Al and Si alloying additions, but also provides much needed exploration and validation data for the structure and property prediction models. Compared to a single FCC phase CoCrFeNi alloy, we show that quinary HEAs with Mn additions up to 42 at.% remained an FCC structure, with Mn or Cu alloying additions had comparable micro hardness, and with other alloying additions along with all senary HEAs destabilizing single phase structures and yielding higher micro hardness. The CALPHAD-based structure predictions with assessed HEA database are superior to Hume-Rothery empirical rules, and the model of Varvenne-based strength predictions provide insights and validated trend for single-phase solid-solution alloys. The HT-HIP-MSA permits reliable and efficient synthesis and exploration of the alloying space for HEAs, and integrating computational models the greater power lies in the expanded use of such a method and its resulting data libraries for targeted design of HEAs.

4. Materials and methods

Traditionally, the HIP process is to fill the alloy powders in a container, vacuum the container under an intermediate temperature to remove the air and moisture, seal the container by welding, and to consolidate powders in Argon under an elevated-temperature and high-pressure condition. In contrast to this one-at-a-time consolidation process, we employ a high-throughput powder-metallurgy synthesis via HIP, where tens or hundreds of alloys can be processed in parallel, and the experimental process is schematically illustrated in Fig. 7. We design and manufacture a honeycomb structure array containing 85 cells by laser additive manufacturing (AM). Different mechanically-milled powder mixtures are loaded in each cell and then HIPed to make a

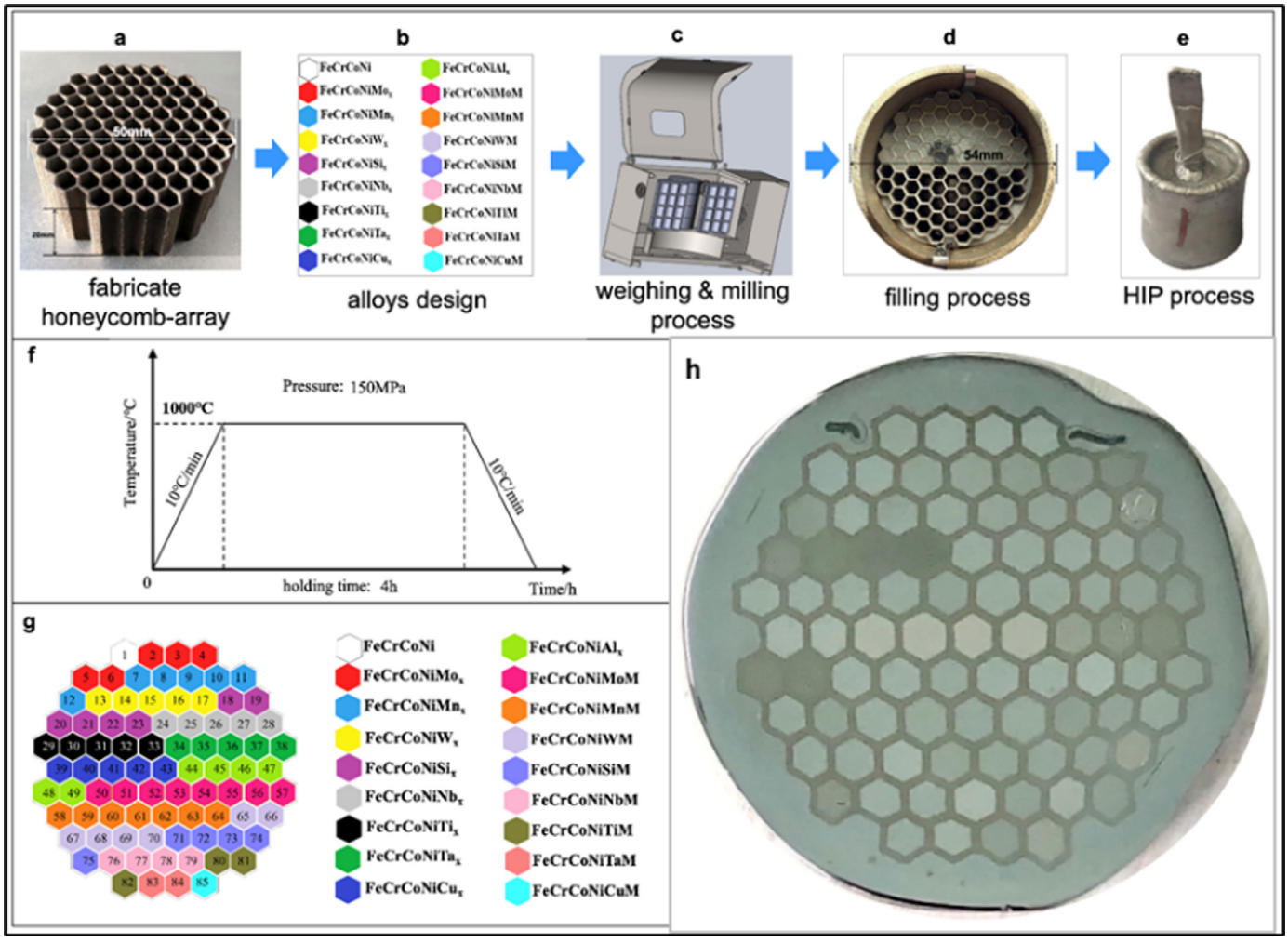

Fig. 7. Honeycomb-array container preparation: (a–e) procedure of honeycomb-sample HIP preparation; (f) detail of HIP process g components of 85 HEAs; (h) honeycomb-structured HEAs library.

discrete-materials-array to enable high throughput characterization and screening alloys efficiently.

The honeycomb-structured sample with 85 cells (Fig. 7(a)) are formed by AM. The gas-atomized pure titanium (Ti) powders (99.9 wt.%,), with the spherical shape and the particle size in the range of 15–45 μm, are used as the starting materials. The parameters of the AM machine (BLT S310, Xi'an Bright Laser Technologies Co., Ltd., China) are conditioned with the laser power of ~ 500 W, laser-spot size of 80 μm, laser scan speed of 1100 mm/s, layer thickness of 50 μm, overlap of 55 μm, and interlayer rotation angle of 67° Furthermore, the AM system is equipped with an automatic powder-layering apparatus, and an inert argon gas protection system. Dimensions of honeycomb arrays are 50 mm in diameter, 20 mm in height, ~ 0.4 mm in wall thickness, and the diagonal length of each cell is 5 mm. Additionally, the honeycomb arrays is placed into a carbon steel container with 50 mm in diameter and 2 mm in thickness.

In designing CoCrFeNi-based HEAs, 13 pure spherical powders (purity> 99.0 wt.%, particle size in the range of 15–45 μm) are selected, including Fe, Cr, Co, Ni, Mo, Mn, W, Si, Nb, Ti, Ta, Cu, and Al (Fig. 7(b)). Four elements of Co, Cr, Fe, and Ni were chosen as the HEA base elements, and the other 9 elements were used as the variable components to for alloys in 1 CoCrFeNi quaternary system, 9 quinary CoCrFeNi-R$_x$, and 39 senary FeCrCoNi-R-A HEAs (Table 1). According to the HEA design, the powders are manually weighted and loaded into ball-mill jars in less than 4 h. After the weighing process, 85 mixture powders were divided into two groups, and each group was milled for 24 h by the high-throughput milling machine designed by the Central South University, which can mill 56 jars at one given time (Fig. 7(c)). In each group, every ball-milling jar with stainless-steel 304 alloy balls rotates at 80 rpm in an airlock condition. After the milling process, 85 mixture powders are manually loaded into each cell of honeycomb arrays (Fig. 7(d)) in about 2 h. After the filling process, the carbon-steel top cover with an exhaust tube is welded onto the steel container.

The welded steel container then goes through the typical processing cycle of HIP, which includes vacuuming the container at room temperature to 10^{-4} Pa, vacuuming the container at 500 °C for 8 h to further remove air and moisture, sealing the exhaust tube on the container to prevent additional air leaking into the container, loading the container into the HIP furnace filling with argon to perform the densification and thermal diffusion at 1000 °C and 150 MPa for 4 h, cooling down to ambient temperature with a controlled rate of 10 °C/min., and removing the container from the HIP furnace (Fig. 7(e)). The detail of the HIP-processing temperature cycle is presented in Fig. 7(f). After the mechanical removal of the bottom and top of the container, the honeycomb-structured HEA library with 85 discrete compositions (Fig. 7(g)) is obtained and metallurgically polished

down to the 1 μm surface finish for further characterization (Fig. 7(h)).

The compositional distribution of the honeycomb-structured HEA library is scanned by the micro X-ray fluorescence (μXRF, Bruker M4 Tornado) with a spot size of 20 μm, step size of 80 μm, scan area of 50 $\times$ 50 mm^2, acquisition time of 100 ms, and total measurement time about 10 h. The compositions of 85 HEAs are assessed by energy-dispersive spectroscopy (EDS, Aztec max 50) at the center of each cell within a $\sim$ 2 $\times$ 2 mm^2 area. Additionally, the diffusion of Ti of the honeycomb structure into the honeycomb cells is measured by EDS. The phase compositions of 85 HEAs are characterized by the micro X-ray diffraction (μXRD, Rigaku) with the parameter of Cu$K\alpha$ radiation between angles of 20° and 100°, and a step size, 2θ, of 0.02°, and spot size of 100 μm. The morphologies of microstructures are observed by scanning electron microscopy (SEM, Zeiss) with a backscatter electron (BSE) mode. The hardness of 85 HEAs is tested at about the center of each cell by the high-throughput micro Vickers hardness (MVH, Qness Q10A+) under a load of 2.0 N.

We calculate composition-phase relationships using the Thermo-Calc Software version 2020a, and the database used is TCHEA4 containing 26 elements [47]. Both are developed by the Thermo-Calc Software AB [47]. We calculate the composition-phase relationship for each design of HEA library using the aim chemistry as inputs, and the equilibrium temperature is set as the HIPing temperature of 1000 °C. The computed equilibrium phases with respect to the design HEA chemistry is tabulated in Table 1.

Declaration of Competing Interest

The authors declare that they have no known competing financial interests or personal relationships that could have appeared to influence the work reported in this paper.

CRediT authorship contribution statement

L. Zhao: Conceptualization, Writing – original draft. **L. Jiang:** Writing – original draft. **W.Y. Zhang:** Writing – original draft. **G.Y. Ji:** Formal analysis. **X. Zhou:** Formal analysis. **W.A. Curtin:** Formal analysis, Writing – original draft. **X.B. Chen:** Writing – review & editing. **P.K. Liaw:** Writing – review & editing. **S.Y. Chen:** Formal analysis, Writing – original draft.

Acknowledgments

This work was financially supported by the National Key Research and Development Program of China (2016YFB0700300). S.Y.C. acknowledges the financial support from National Natural Science Foundation of China (No. 52001271). The authors thank Mr. Yuji Shiramata from Rigaku Co. Japan for the experiments of μ-XRD and Ph.D. Qiqi Yan from Bruker Co. China for the experiments of μ-XRF. P. K. Liaw very much appreciates the supports from (1) the National Science Foundation (DMR-1611180 and 1809640) with program directors, Drs. J. Yang, G. Shiflet, and D. Farkas and (2) the US Army Research Office (W911NF-13-1-0438 and W911NF-19-2-0049) with program managers, Drs. M.P. Bakas, S.N. Mathaudhu, and D.M. Stepp. X.Z. and W.C. thank the Swiss National Science Foundation for support of this work by project "Harnessing atomic-scale randomness: design and optimization of mechanical performance in High Entropy Alloys (Project 200021_118198/1).

Data availability

All data included in this study are available from the corresponding author on reasonable request.

Supplementary materials

Supplementary material associated with this article can be found, in the online version, at doi:10.1016/j.jmst.2021.09.031.

References

[1] B. Cantor, Prog. Mater. Sci. 120 (2020) 100754.
[2] J.W. Yeh, S.K. Chen, S.J. Lin, J.Y. Gan, T.S. Chin, T.T. Shun, C.H. Tsau, S.Y. Chang, Adv. Eng. Mater. 6 (2004) 299–303.
[3] Y. Lederer, C. Toher, K.S. Vecchio, S. Curtarolo, Acta Mater. 159 (2018) 364–383.
[4] O.N. Senkov, J.D. Miller, D.B. Miracle, C. Woodward, Nat. Commun. 6 (2015) 6529.
[5] F.G. Coury, K.D. Clarke, C.S. Kiminami, M.J. Kaufman, A.J. Clarke, Sci. Rep. 8 (2018) 8600.
[6] C. Wen, Y. Zhang, C. Wang, D. Xue, Y. Bai, S. Antonov, L. Dai, T. Lookman, Y. Su, Acta Mater. 170 (2019) 109–117.
[7] J.M. Rickman, H.M. Chan, M.P. Harmer, J.A. Smeltzer, C.J. Marvel, A. Roy, G. Balasubramanian, Nat. Commun. 10 (2019) 2618.
[8] G. Bracq, M. Laurent-Brocqa, C. Varvenne, L. Perrière, W.A. Curtin, J.M. Joubert, I. Guillot, Acta Mater. 177 (2019) 266–279.
[9] T. Borkar, B. Gwalani, D. Choudhuri, C.V. Mikler, C.J. Yannetta, X. Chen, R.V. Ramanujan, M.J. Styles, M.A. Gibson, R. Banerjee, Acta Mater. 116 (2016) 63–76.
[10] A. Kauffmann, M. Stüber, H. Leiste, S. Ulrich, S. Schlabach, D.V. Szabó, S. Seils, B. Gorr, H. Chen, H.J. Seifert, M. Heilmaier, Surf. Coat. Technol. 325 (2017) 174–180.
[11] K.G. Pradeep, C.C. Tasan, M.J. Yao, Y. Deng, H. Springer, D. Raabe, Mater. Sci. Eng. A 648 (2015) 183–192.
[12] Z. Li, A. Ludwig, A. Savan, H. Springer, D. Raabe, J. Mater. Res. 33 (2018) 3156–3169.
[13] Q. Ding, Y. Zhang, X. Chen, X. Fu, D. Chen, S. Chen, L. Gu, F. Wei, H. Bei, Y. Gao, M. Wen, J. Li, Z. Zhang, T. Zhu, R.O. Ritchie, Q. Yu, Nature 574 (2019) 223–227.
[14] B. Gludovatz, A. Hohenwarter, D. Catoor, E.H. Chang, E.P. George, R.O. Ritchie, Science 345 (2014) 1153–1158.
[15] T. Yang, Y.L. Zhao, Y. Tong, Z.B. Jiao, J. Wei, J.X. Cai, X.D. Han, D. Chen, A. Hu, J.J. Kai, K. Lu, Y. Liu, C.T. Liu, Science 362 (2018) 933–937.
[16] D.B. Miracle, Nat. Commun. 10 (2019) 1805.
[17] Y.H. Jo, S. Jung, W.M. Choi, S.S. Sohn, H.S. Kim, B.J. Lee, N.J. Kim, S. Lee, Nat. Commun. 8 (2017) 15719.
[18] Z. Li, K.G. Pradeep, Y. Deng, D. Raabe, C.C. Tasan, Nature 534 (2016) 227–230.
[19] S. Chen, H.S. Oh, B. Gludovatz, S.J. Kim, E.S. Park, Z. Zhang, R.O. Ritchie, Q. Yu, Nat. Commun. 11 (2020) 826.
[20] Y. Shi, B. Yang, X. Xie, J. Brechtl, K.A. Dahmen, P.K. Liaw, Corros. Sci. 119 (2017) 33–45.
[21] M.R. He, S. Wang, S. Shi, K. Jin, H. Bei, K. Yasuda, S. Matsumura, K. Higashida, I.M. Robertsona, Acta Mater. 126 (2017) 182–193.
[22] R.L. Livezey, Am. Midl. Nat. 49 (1953) 937.
[23] M.S. Lucas, G.B. Wilks, L. Mauger, J.A. Muñoz, O.N. Senkov, E. Michel, J. Horwath, S.L. Semiatin, M.B. Stone, D.L. Abernathy, E. Karapetrova, Appl. Phys. Lett. 100 (2012) 251907.
[24] F. Otto, Y. Yang, H. Bei, E.P. George, Acta Mater. 61 (2013) 2628–2638.
[25] C. Li, J.C. Li, M. Zhao, Q. Jiang, J. Alloy. Compd. 504 (2010) S515–S518.
[26] F. He, Z. Wang, P. Cheng, Q. Wang. J. Li, Y. Dang, J. Wang, C.T. Liu, J. Alloy. Compd. 656 (2016) 284–289.
[27] C. Ai, F. He, M. Guo, J. Zhou, Z. Wang, Z. Yuan, Y. Guo, Y. Liu, L. Liu, J. Alloy. Compd. 735 (2018) 2653–2662.
[28] T.T. Shun, L.Y. Chang, M.H. Shiu, Mater. Sci. Eng. A 556 (2012) 170–174.
[29] L. Jiang, Y. Lu, Y. Dong, T. Wang, Z. Cao, T. Li, Intermetallics 44 (2014) 37–43.
[30] H. Song, F. Tian, Q.M. Hu, L. Vitos, Y. Wang, J. Shen, N. Chen, Phys. Rev. Mater. 1 (2017) 023404.
[31] X. Yang, Y. Zhang, Mater. Chem. Phys. 132 (2012) 233–238.
[32] I. Toda-Caraballo, P.E.J. Rivera-Díaz-del-Castillo, Intermetallics 71 (2016) 76–87.
[33] M. Calvo-Dahlborg, S.G.R. Brown, J. Alloy. Compd. 724 (2017) 353–364.
[34] https://thermocalc.com/content/uploads/Documentation/Databases/Thermodynamic/tchea4-technical-info.pdf.
[35] C.M. Lin, H.L. Tsai, H.Y. Bor, Intermetallics 18 (2010) 1244–1250.
[36] J.B. Cheng, X.B. Liang, Z.H. Wang, B.S. Xu, Plasma Chem. Plasma Process. 33 (2013) 979–992.
[37] Z. Niu, J. Xu, T. Wang, N. Wang, Z. Han, Y. Wang, Intermetallics 112 (2019) 106550.
[38] H. Jiang, L. Jiang, D. Qiao, Y. Lu, T. Wang, Z. Cao, T. Li, J. Mater. Sci. Technol. 33 (2017) 712–717.
[39] G. Michael, J.W. Yeh, P.K. Liaw, Y. Zhang, High-Entropy Alloys, Springer, 2016.
[40] C. Varvenne, G.P.M. Leyson, M. Ghazisaeidi, W.A. Curtin, Acta Mater. 124 (2017) 660–683.
[41] S. Nag, C. Varvenne, W.A. Curtin, Model. Simul. Mater. Sci. Eng. 28 (2020) 025007.
[42] G. Bracq, M. Laurent-Brocq, C. Varvenne, L. Perrière, W.A. Curtin, J.M. Joubert, I. Guillot, Acta Mater. 177 (2019) 266–279.
[43] B. Yin, W.A. Curtin, NPJ Comput. Mater. 5 (2019) 1–7.
[44] Z. Wu, H. Bei, F. Otto, G.M. Pharr, E.P. George, Intermetallics 46 (2014) 131–140.
[45] C. Varvenne, A. Luque, W.A. Curtin, Acta Mater. 118 (2016) 164–176.
[46] C. Varvenne, W.A. Curtin, Scr. Mater. 138 (2017) 92–95.
[47] Thermo-Calc Software and Database, https://thermocalc.com/.
[48] T.T. Shun, L.Y. Chang, M.H. Shiu, Mater. Charact. 70 (2012) 63–67.

[49] Z. Niu, Y. Wang, C. Geng, J. Xu, Y. Wang, J. Alloy. Compd. 820 (2020) 153273.
[50] X. Qiu, J. Mater. Res. Technol. 9 (2020) 5127–5133.
[51] M.J. Yao, K.G. Pradeep, C.C. Tasan, D. Raabe, Scr. Mater. 5-8 (2014) 72–73.
[52] G. Cui, B. Han, Y. Yang, M. Li, J. Li, Surf. Coat. Technol. 381 (2020) 125182.
[53] A.C. Fan, J.H. Li, M.H. Tsai, J. Alloy. Compd. 823 (2020) 153524.
[54] K.B. Zhang, K.B. Zhang, Z.Y. Fu, J.Y. Zhang, W.M. Wang, H. Wang, Y.C. Wang, Q.J. Zhang, J. Shi, Mater. Sci. Eng. A 508 (2009) 214–219.
[55] A. Verma, P. Tarate, A.C. Abhyankar, M.R. Mohape, D.S. Gowtam, V.P. Deshmukh, T. Shanmugasundaram, Scr. Mater. 161 (2019) 28–31.
[56] W.L. Wang, Z.H.J. Kong, J. Alloy. Compd. 853 (2020) 156451.
[57] Z. Xu, Z. Li, Y. Tong, W. Zhang, Z. Wu, J. Mater. Sci. Technol. 60 (2021) 35–43.
[58] C.M. Lin, H.L. Tsai, Intermetallics 19 (2011) 288–294.
[59] Y. Lv, R. Hu, Z. Yao, J. Chen, D. Xu, Y. Liu, X. Fan, Mater. Des. 132 (2017) 392–399.
[60] N. Haghdadi, T. Guo, A.A. Ghaderi, P.D. Hodgson, M.R. Barnett, D.M. Fabijanic, Wear 428-429 (2019) 293–301.
[61] G. Liu, L. Liu, X. Liu, Z. Wang, Z. Han, G. Zhang, A. Kostka, Intermetallics 93 (2018) 93–100.
[62] W.R. Wang, W.L. Wang, S.C. Wang, Y.C. Tsai, C.H. Lai, J.W. Yeh, Intermetallics 26 (2012) 44–51.
[63] C.D. Gómez-Esparza, R. Martínez-Sánchez, A.R-G Duarte-Moller, C.A. Microsc. Microanal. 25 (2019) 2416–2417.
[64] J. Zhu, H.M. Fu, H.F. Zhang, A.M. Wang, H. Li, Z.Q. Hu, Mater. Sci. Eng. A 527 (2010) 6975–6979.
[65] S.A. Uporov, R.E. Ryltsev, V.A. Bykov, S.K. Estemirova, D.A. Zamyatin, J. Alloy. Compd. 820 (2020) 153228.
[66] A. Kumar, A.K. Swarnakar, A. Basu, M.J. Chopkar, J. Alloy. Compd. 748 (2018) 889–897.
[67] J. Zhu, H.M. Fu, H.F. Zhang, A.M. Wang, H. Li, Z.Q. Hu, Mater. Sci. Eng. A 527 (2010) 7210–7214.
[68] J. Cheng, D. Liu, X. Liang, B. Xu, Acta Metall. Sin. Engl. Lett. 27 (2014) 1031–1037.
[69] X.F. Wang, Y. Zhang, Y. Qiao, G.L. Chen, Intermetallics 15 (2007) 357–362.
[70] J. Liu, H. Liu, P. Chen, J. Hao, Surf. Coat. Technol. 361 (2019) 63–74.
[71] X.W. Qiu, J. Alloy. Compd. 555 (2013) 246–249.